

# Statistical properties of ultraluminous IRAS galaxies from an HST imaging survey

J. Cui

Beijing Astronomical Observatory, Chinese Academy of Sciences  
Electronic mail: cuijun@bac.pku.edu.cn

X.-Y. Xia

Dept. of Physics, Tianjin Normal University  
Electronic mail: xyxia@bac.pku.edu.cn

Z.-G. Deng

Dept. of Physics, Graduate School, Chinese Academy of Sciences  
Electronic mail: dzg@bac.pku.edu.cn

S. Mao

Jodrell Bank Observatory, University of Manchester  
Electronic mail: smao@jb.man.ac.uk

Z.-L. Zou

Beijing Astronomical Observatory, Chinese Academy of Sciences  
Electronic mail: zzl@class1.bao.ac.cn

## ABSTRACT

We perform photometric measurements on a large *HST* snapshot imaging survey sample of 97 ultraluminous infrared galaxies (ULIRGs). We select putative nuclei from bright clumps in all the sample targets, mainly based on a quantitative criterion of *I*-band luminosity as well as the global and local morphological information. All the sources are then classified into three categories with multiple, double and single nucleus/nuclei. The resultant fractions of multiple, double and single nucleus/nuclei ULIRGs are 18%, 39% and 43%, respectively. This supports the multiple merger scenario as a possible origin of ULIRGs, in addition to the commonly-accepted pair merger model. Further statistical studies indicate that the AGN fraction increases from multiple (36%) to double (65%) and then to single (80%) nucleus/nuclei ULIRGs. For the single nucleus category, there is a high luminosity tail in the luminosity distribution, which corresponds to a Seyfert 1/QSO excess. This indicates that active galactic nuclei tend to appear at final merging stage. For multiple/double nuclei galaxies, we also find a high fraction of very close nucleus pairs (e.g., 3/4 for those separated by less than 5 kpc). This strengthens the conclusion that systems at late merging phase preferentially host ULIRGs.

*Subject headings:* galaxies: nuclei — galaxies: star clusters — galaxies: interactions — galaxies: evolution — infrared: galaxies

## 1. Introduction

For more than ten years, much effort has been made to understand the properties of ultraluminous infrared galaxies (hereafter ULIRGs, see Sanders & Mirabel 1996 for a review), and it is now widely accepted that this population of objects represents an important evolutionary stage triggered by strong galaxy interactions/mergers, especially major mergers between gas-rich spirals with mass ratio smaller than 3:1 (e.g., Bendo & Barnes 2000). These ULIRGs may represent an important stage in the formation of QSOs and powerful radio galaxies, as well as an essential step in the formation of elliptical galaxies (e.g., Sanders *et al.* 1988a; Melnick & Mirabel 1990). Although the nature of ULIRGs is believed to be understood in general terms, it is still not clear whether these objects originate from the interactions/mergers of galaxy pairs or galaxy groups.

On the theoretical side, numerical simulations have successfully reproduced global and even some fine structural properties of elliptical-like galaxies as the results of pair mergers (e.g., Toomre & Toomre 1972; White 1978; Farouki & Shapiro 1982; Negroponte & White 1983; Barnes 1992; Hernquist 1992; Heyl *et al.* 1994; Barnes & Hernquist 1996; Weil & Hernquist 1996; Walker *et al.* 1996; Mihos & Hernquist 1994; Springel & White 1998). However, the pair merger model can not account for all the observed properties of elliptical galaxies, which leads people to consider the multiple merger scenario (e.g., Mamon 1987; Barnes 1984, 1985, 1989; Schweizer 1989; Weil & Hernquist 1996). In fact, numerical simulations of multiple mergers do produce remnants different from those produced by pair mergers in both morphological and kinematic properties (Weil & Hernquist 1996). On the other hand, there is increasing observational evidence to support the multiple merger scenario. For example, the co-existence of three OH maser components in the typical ULIRG Arp 220 is of possible multiple merger origin (Taniguchi & Shioya 1998). And Lipari *et al.* (1999) reported detailed evidence for multiple merger in the luminous infrared galaxy NGC 3256 based on high resolution imaging by *HST* and *ESO-NTT*. Furthermore, Borne *et al.* (1999a, 1999b) carried out a thorough ULIRGs imaging survey by *HST* WFPC2/NICMOS, of which they displayed about 20 ULIRGs either with multiple nuclei or representing interacting groups (Borne *et al.* 2000). Based on their results, Borne *et al.* (2000) suggested that a possible progenitor of the ULIRG population is compact groups of galaxies.

In optical and near infrared images of luminous merging galaxies, such as ULIRGs, there always exist many kpc or sub-kpc scale intense star-forming regions (Lutz 1991; Ashman & Zepf 1992; Holtzman *et al.* 1992; Zepf & Ashman 1993; Surace & Sanders 1999). It has often been argued that these star clusters may form during violent collisions between gas clouds induced by tidal interactions (Hutchings 1995), and that their formation may be linked directly to intense starbursts occurring at the very centers of ULIRGs (Taniguchi *et al.* 1998). Compared

with numerous star-forming regions in nearby interacting systems or starburst galaxies such as NGC 4038/9 (Whitmore & Schweizer 1995), NGC 3310 and NGC 2415 (Gallagher *et al.* 2000), star clusters in ULIRGs are generally more luminous and massive, with bolometric luminosity,  $L_{\text{bol}}$ , sometimes ranging up to  $2 \times 10^9 L_{\odot}$  and their masses are typically a factor of 100 greater than Galactic globular clusters (Scoville *et al.* 1999). A likely explanation is that these objects are associations of star clusters seen in more nearby systems (Surace *et al.* 1998), since the typical intercluster separation in nearby starburst regions is too small ( $\leq 18$  pc, see Meurer 1995) to be resolved at high redshift. Since both such star cluster associations and galactic nuclei may appear as local brightness enhancements on ULIRG images and the luminosities of the largest associations can be comparable with those of galactic nuclei, it is necessary to find a feasible criterion to distinguish these two types of objects of different physical nature. Hereafter for convenience, we adopt a nomenclature in which the luminous star-forming regions alone are named as *knots* or *star cluster associations*, while they are named as *clumps* together with galactic nuclei.

Although there exists observational evidence for multiple merging from investigations on both individual targets and large samples, most of these works are based on qualitative analysis and use somewhat subjective criteria. Therefore, it is important to investigate this issue on a quantitative basis; this becomes more requisite considering the possibility of mistaking star cluster associations as galactic nuclei in ULIRGs, since they are similar in many aspects. This comprises the main subject of the present paper; in our work, we perform a careful photometric analysis on a large *HST* snapshot imaging survey sample of ULIRGs (Borne *et al.* 1999a, 1999b), in order to find evidence for multiple merger based primarily on a quantitative criterion of *I*-band luminosity. On the other hand, there are still no detailed comparisons of multiple mergers with other populations of ULIRGs (e.g., double mergers and single nucleus galaxies, see Sec. 5). This provides the second motivation for our paper. The structure of this paper is as follows: Sec. 2 includes basic information about the ULIRG sample and their observations. In Sec. 3, we describe details of our data reduction. In Sec. 4, we detail our quantitative criterion for identifying putative galactic nuclei. In Sec. 5, we present our main results, i.e., evidence for multiple mergers and a comparison of different ULIRG populations. Finally, we discuss and summarize our results in Sec. 6. Throughout this paper we assume an Einstein-de Sitter cosmology ( $\Omega_0 = 1$ ) and adopt  $H_0 = 75 \text{ km s}^{-1} \text{ Mpc}^{-1}$ . At the typical redshift ( $z = 0.1$ ) of the sample galaxies,  $0.1''$  (about 1 pixel) corresponds to roughly 200 pc.

## 2. Sample and observations

For our purpose, we use archive data from an *HST* snapshot imaging survey of ULIRGs (Borne *et al.* 1999a, 1999b). The sample images were taken using the *Wide Field Planetary Camera 2* (WFPC2) in the *I*-band pass (F814W), including 120 targets all centered in the WF3 chip, of which the resolution is  $0.0996''$  per pixel and the FOV is  $800 \times 800$  pixels. For each target in this survey, two 400s exposures were taken. Most of the observed targets were selected from

the QDOT sample (Leech *et al.* 1994; Lawrence *et al.* 1999), the rest were selected from the brightest samples of Sanders *et al.* (1998a, 1998b) and Melnick & Mirabel (1990). Apart from some sources which are saturated, mis-focused or contaminated by bright foreground stars, we make use of 97 independent targets for our study. In addition, all these sources are selected to possess projected nuclear separations less than 20 kpc (for galaxies with more than two putative nuclei, only minimum nuclear separations are considered). This is because generally speaking, *strong interactions* between galaxies are induced in systems with nuclear separations below this value, i.e., the distance adequate for two interacting galaxies to obtain a substantial disturbance down to their nuclear radii of 1-2 kpc within the lifetime of the encounter (e.g., Lin *et al.* 1988). Basic information for all the targets is listed in Table 1 in the order of increasing *RA*, including *HST* visit No., target name, *RA*, *Dec*, redshift, far-infrared luminosity and our classification (see Sec. 5). The redshifts of these objects range from 0.04 to 0.35.

### 3. Data reduction

The sample images were first preprocessed through the *standard Space Telescope Science Institute* (STScI) pipeline, using a standard WFPC2-specific calibration algorithm and the best available calibration files (Holtzman *et al.* 1995). The preprocessing consists of mask and analog-to-digital correction, bias and dark subtraction, as well as flat-fielding, etc.. Our post-pipeline calibrations include detection and removal of warm pixels and cosmic ray events. The additional steps of data reduction are discussed below.

#### 3.1. Selection for clumpy structures

We use the standard *IRAF* task *imexamine* to carefully browse the sources in the ULIRG sample. For each target, three plots are displayed and compared with each other – the contour plot, the surface plot and the snapshot image. The image is adjusted to different greyscale levels until it renders the best visualization. The surface plot is always checked from several different angles to get a full view. A set of ceiling values are tried until the contour plots yield a clear view of the weak structures of the targets. By careful comparison, common local brightness enhancements appearing on each plot are marked as putative clumps. On surface plots, such clump candidates are identified on the basis of detectable brightness peaks; while on contour plots, they are identified on the basis of closed isophotal contours. As for snapshot images, it is hard to resolve them by greyscale adjustment to present all the clumps detectable in surface or contour plots, except for those very bright or compact clumps with high signal-to-noise ratio. However, snapshot images are especially useful in that interacting structures in ULIRGs are more perceptible in these plots, and such structures are very useful for determining whether or not several distinct separate regions near the target position belong to a single dynamically related system. This is done based on the existence of detectable tidal streamers connecting separate

regions. Otherwise, we identify the object nearest to the IRAS position as the target we need, and its nearby objects are considered to be either foreground or background ones (see also Sec. 6.1). Hence our method will give a (conservative) lower limit on the fraction of multiple merger objects.

In order to distinguish true physical clumps from Poisson fluctuation peaks in the images, we make rough FWHM (full width at half maximum) measurements on the marginally detectable brightness peaks, and fluctuations are identified to be those peaks with FWHMs smaller than the typical value of observed PSF (point spread function) of *HST* WF3 chip with F814W filter. Furthermore, it can not be ruled out that foreground stars may coincidentally fall onto the target and are thus mistaken as ULIRG clumps. A rough estimation of this probability is made using all the 7 ULIRGs in the sample at relatively low galactic latitude (i.e.,  $|b| < 15^\circ$ ). We use the standard *IRAF* task *daofind* to search for star-like objects in these 7 ULIRGs which are brighter than the minimum clump flux we have identified in the sample (about 22.5 mag). And by multiplying the star number by the ratio of the target area to the whole field area, we obtain an average contamination number of about 0.1 for one galaxy, hence the influence of star contamination on our results is negligible. Here the area occupied by each target is determined by counting the number of pixels with ADU values at least  $3\sigma$  above the sky background. This is a conservative upper limit, since the sub-sample we treat is contaminated by foreground stars to the greatest extent due to low galactic latitude.

### 3.2. Surface photometry

We perform surface photometric measurements on the selected clumps to determine their *I*-band fluxes and luminosities. For well-separated clumps, we apply standard aperture photometry programs in which aperture widths are set to different values according to their actual sizes, ranging from  $0.2''$  to  $1.0''$ . The size is estimated from the surface brightness profile when it reaches an approximately constant value, i.e., the local background value. In addition, estimates are made of the underlying background galaxy flux by using the mean of the pixels in a 1-pixel annulus immediately outside the photometric aperture. However, some clumps in ULIRGs are so close that their profiles overlap notably, hence standard procedures do not function well. In such cases we perform surface photometry in the following way: we apply a large aperture size to encircle all the overlapping clumps and the magnitude,  $m$ , measured this way is considered to be the combined *I*-band magnitude of encircled objects; at the same time we apply a small aperture size to measure the magnitude,  $m'$ , of the protrudent part (i.e., non-overlapping region) of each encircled clump, and the flux ratio of these parts is approximated as that of the corresponding true clumps, assuming that these overlapping clumps possess similar profiles. Using  $m$ ,  $m'_1$  and  $m'_2$ , we can estimate the true magnitude of clumps from the following expression,

$$m_1 = m + 2.5 \log \left( 1 + 10^{\frac{m'_1 - m'_2}{2.5}} \right), \quad (1)$$

$$m_2 = m + 2.5 \log \left( 1 + 10^{\frac{m'_2 - m'_1}{2.5}} \right). \quad (2)$$

In all our surface photometry, the photometric calibration is performed using published photometric solutions for WFPC2 and F814W filter (Holtzman *et al.* 1995).

Simulations are performed in order to estimate the uncertainty of the measured fluxes for overlapping clumps. Using the standard *IRAF* task *mkobjects*, we automatically produce two objects (artificial clumps) with different flux ratios and separations. Their FWHMs are fixed to be 5 pixels. For convenience, only de Vaucouleurs brightness profiles are considered. In addition, Poisson noise is added to the simulated objects and the effects of detector gain, readout and PSF are all modeled using the appropriate parameters for the *HST* WF3 chip. Table 2 lists details of each simulation run. From the table, we can see that the largest photometric uncertainty occurs when the separations between clumps are small and the corresponding magnitude difference of simulated clumps is high. Since there are no overlapping clumps in this sample with very different *I*-band magnitude, the typical photometric uncertainty introduced by our technique is less than 0.2 mag, and the largest uncertainty in our measurements, corresponding to run 12 in Table 2, is around 0.5 mag. Hence the introduced photometric uncertainty does not affect our results significantly.

#### 4. Identification of putative nuclei

As mentioned in Sec. 1, one of the remarkable features of ULIRGs is that there always exist many kpc or sub-kpc scale luminous clumpy structures; and the key issue in our work is to distinguish putative nuclei from star cluster associations. It is found that typical masses for both galactic nuclei in ULIRGs and the giant elliptical cores are several times of  $10^9 M_\odot$  (Sakamoto *et al.* 1999; Lauer 1985). This is typically larger than the mass found for star formation knots. In detailed studies of nearby starburst galaxies such as M82 (de Grijs *et al.* 1999), no star-forming knots have been observed to possess masses as high as  $10^9 M_\odot$ . And for the nearest ULIRG, Arp 220, its most massive knot was found to possess a mass of  $6.6 \times 10^8 M_\odot$  (Shioya *et al.* 2000). On the theoretical side, complexes with masses greater than  $10^9 M_\odot$  may suffer from disintegration (Noguchi 1999). In addition, Taniguchi *et al.* (1998) suggested that a large mass of  $10^9 M_\odot$  corresponds to a maximum star formation efficiency of 1 for knots evolving from superclouds in gravitationally unstable gas disks. Since the real star formation efficiency must be smaller (e.g., 0.1 from observations of the Galaxy), observed knots are always less massive than  $10^9 M_\odot$ . Given these, we conservatively adopt  $1 \times 10^9 M_\odot$  as the lower mass limit to pick out putative nuclei from bright clumps in the first step.

To express the above threshold in an observational quantity, the lower mass limit is converted to *B*-band luminosity using a constant mass-to-light ratio of 6.5 appropriate for spheroids (Fugukita *et al.* 1998). And the resultant value of  $1.54 \times 10^8 L_\odot$  corresponds to  $M_B = -15.0$ . Adopting the statistical results of Surace *et al.* (1998) that the typical *B – I* color index for

putative nuclei in ULIRGs is 2.0 with a root mean square of 0.7, we obtain the lower  $M_I$  limit of  $-17.0$  mag as a quantitative criterion to pick out putative nuclei from bright clumps. This is consistent with the argument that bright knots may have an upper luminosity limit for intense star-formation in a star cluster (Hutchings 1995).

We caution that this quantitative criterion may not be sufficient to pick out ULIRG nuclei in some cases. This is mainly due to two reasons. First, the brightest knots and relatively faint nuclei in ULIRGs may have comparable luminosities. Second, the nuclear and circumnuclear regions of ULIRGs are heavily obscured – as a result, a single nucleus may emerge as multiple condensations due to complex obscuration patterns. In order to eliminate the influences of these two effects, we take further morphological considerations, which are discussed below.

#### 4.1. Morphological considerations

Generally speaking, in order to distinguish those extremely bright knots from the putative nuclei, color information is needed (e.g., Surace *et al.* 1998, Scoville *et al.* 1999). However, we do not incorporate color index in this paper, because the ULIRGs imaging survey sample we used was performed only in the  $I$ -band. In addition, the results of  $B - I$  color show that this index covers a rather wide range from  $-0.3$  to  $5.2$  for star-forming knots (Surace *et al.* 1998). Considering the relatively narrow span of  $0.5$  to  $3.1$  for putative nuclei (Surace *et al.* 1998), it is obvious that knots can be either bluer or redder than nuclei, as was also pointed out by Hutchings (1995). Therefore, the color index is not an ideal indicator to distinguish putative nuclei from star formation knots.

On the other hand, although the luminosities of some super star clusters are comparable to or even greater than those of putative galactic nuclei, this luminosity overlap is relatively insignificant compared with the overlap of color index. Among all the 57 knots in Surace’s sample, less than 30% are brighter than our  $I$ -band luminosity threshold of  $-17.0$  mag (see Fig 1 for the magnitude distribution of all these 57 knots). Furthermore, we suspect that some of these very bright knots in Surace’s sample are possible galactic nuclei (see Sec. 6.1).

Star-forming knots with large  $I$ -band luminosities (i.e., comparable to those of putative nuclei) may also exist in the current ULIRG sample. To rule them out on a single wavelength basis, we take into account the dynamical information provided by interacting signatures of the targets. This technique led Lipari *et al.* (1999) to detect three galactic nuclei in NGC 3256 based on *HST* and *ESO-NTT* observations. Therefore, after applying the quantitative criterion of  $M_I$ , we carefully examine the local (such as nuclear arms and disks) as well as global (such as tidal tails, plumes, rings) environments of the sample targets to confirm whether or not clumps brighter than  $M_I = -17.0$  are actual descendents of progenitor bulges. Both numerical simulations and observations show that each piece of such signatures is connected to at least one nucleus residing at its starting position (e.g., Toomre & Toomre 1972; Wright 1972). Because of this, some very bright clumps (i.e., brighter than  $-17.0$  mag) are still treated as massive star-forming regions

if they are located in the outer parts of the sample targets (e.g., at the tips of tail structures). Such objects are more likely to be tidal galaxies produced by merging (Fellhauer & Kroupa 2000), hence they are not included in our work. In our sample, there are 22 such clumps brighter than  $-17.0$  mag in the  $I$ -band which are removed due to these morphological considerations. Compared with the total number of putative nuclei of nearly 200, this step, although important, should not affect our statistical results.

This morphological consideration works fairly well, since in most of our cases, such interacting signatures are easy to identify and their geometrical connections to bright clumps in the same images are explicit. Thus this technique eliminates at least some of the uncertainties in our identification of putative nuclei due to the luminosity overlaps between nuclei and knots. However, it should still be notified that some levels of subjectivity cannot be avoided in the morphological considerations mainly due to two reasons. The first is that faint interacting signatures may be buried in the background noise and are not detectable, especially for the targets at relatively high redshift. The second is that the starting positions of these structures are unclear in some cases. e.g., it is not clear how to pick out the putative nuclei from a group of clumps located along a tidal ring, purely from morphological signatures. Since some features of interacting systems may be due to quirks of pre-encounter disks and do not lead to fundamental insights (Barnes 1999), it is not surprising that we sometimes have ambiguous circumstances. In such cases, we simply apply our quantitative magnitude criterion to identify putative nuclei.

## 4.2. Obscuration effects

Since the high far-infrared luminosity of ULIRGs results from thermal re-radiation from dust (Sanders & Mirabel 1996), there is no doubt that ULIRG morphologies tend to be affected by dust obscuration. Images taken at longer wavelength are needed to examine the extent to which the morphologies of the sample targets are influenced. For the near infrared images of 9 LIGs plus 15 ULIRGs taken by HST NICMOS camera (at 1.1, 1.6 and 2.2  $\mu\text{m}$ ), it was stated that although new interacting features as well as new super star clusters could be found at longer wavelengths, no new nuclei were seen in these images (Scoville *et al.* 1999). This fact suggests that global morphologies are not greatly affected by dust obscuration effects at optical wavelengths, and hence our identification of putative nuclei should be reasonably secure.

In fact, to further minimize the above-mentioned effect, some targets in the sample were treated separately, as in the cases of IR09427+1929, IR06361–6217 and IR04024–8303, etc. Although these targets show signs of separate nucleus components, the combined shapes of their brightness profiles and loss of any nearby signatures of on-going interactions suggest that they are more likely to be a single nucleus split by a foreground dust lane. Surace *et al.* (1998) have reported such cases in their warm ULIRG sample, e.g., IR05189–2524. This procedure is also consistent with Borne *et al.*'s criterion that only cases with clearly separated optically luminous galactic components were selected (Borne *et al.* 2000).

To summarize, the identification of putative galactic nuclei in our reduction includes two steps. The first step is to apply directly an  $I$ -band luminosity criterion, in which all the ULIRG clumps brighter than  $-17.0$  mag were considered as nucleus candidates for further consideration. The second step is to include morphological information (primarily, the existence and characteristics of tidal features), in order to remove some super star clusters with  $I$ -band luminosities comparable to those of putative nuclei. Only nuclei which pass through these two criteria are considered as putative galactic nuclei. In the next section, we present statistical analyses of this group of objects.

## 5. Results

Based on the quantitative criterion discussed in Sec. 4 as well as morphological structures, we pick out all the putative galactic nuclei from clumpy structures in each sample galaxy. And all the 97 ULIRGs can be classified as three categories according to the number of their nuclei:

- Multiple nuclei ULIRGs (multiple mergers)
- Double nuclei ULIRGs (double/pair mergers)
- Single nucleus ULIRGs (single remnants)

Note that for the double nuclei category, two galaxies with projected nuclear separations of more than 20 kpc are excluded (IR13156+0435 and IR15168+0045). Hence these three categories compose a nearly complete sample of *strong interacting systems and their remnants with ultraluminous far-infrared luminosities*. Note that here we adopt a working assumption that every nucleus present in merging systems corresponds to a single progenitor nucleus (bulge), i.e., we assume that dynamical processes (such as tidal disruption) cannot produce compact regions with masses beyond  $10^9 M_{\odot}$ . We caution that this assumption, while reasonable, needs to be verified using numerical simulations.

Photometric results of all the putative nuclei in the sample are listed in Tables 3, 4 and 5 for the three categories, respectively, including positions and  $I$ -band absolute magnitudes. In all these tables, nucleus positions are expressed by  $RA$  and  $Dec$  relative to the corresponding target positions given in Table 1, which are fixed to pixel coordinate of (420, 424) in the *HST* WF3 chip. For multiple and double mergers (see Tables 3 and 4), projected nuclear separations as well as luminosity ratios are included, and we only give minimum separations for the multiple nuclei category. Furthermore, some basic information about the targets are also listed in these tables, including tail lengths, brief comments on morphology and available spectral types.

Our results show that among all the 97 ULIRGs of the treated sample, 17 are multiple nuclei systems, 38 are double nuclei systems, while the remaining 42 have only one identifiable galactic nucleus. This gives plausible fractions of ULIRGs with multiple, double and single nucleus/nuclei

as 18%, 39% and 43%, respectively. These results evidently support the multiple merger scenario as a possible origin of ULIRGs, in addition to the widely-accepted pair merger picture. This argument was put forward by Borne *et al.* (2000) based on the same sample. However, our results are obtained in a more objective way due to our mainly quantitative criterion. Comparisons between Borne’s results and ours are presented in Sec. 6.2. In addition, further statistical studies on this large sample reveal some differences among the three ULIRG categories in our taxonomy, some of which give hints to a possible evolutionary sequence from multiple mergers to double mergers and then to single merger remnants (hereafter M→D→S sequence, see Sec. 5.2). These results not only support our classification scheme, but also give some insights into the dynamics of galaxy interactions/mergers (see Sec. 6.2).

Besides putative nuclei, there often exist several bright knots in most of the sample galaxies. One of the significant characteristics of these bright knots is that they tend to distribute around nuclear regions, or in regions between/among separate nuclei. This is consistent with the argument that star-forming concentrations are preferentially situated along the overlapping areas of interacting galactic disks (Scoville *et al.* 1999). Besides these nuclear knots, there are also cases with circum-nuclear knots, or even with knots residing at the tips of tidal tails. As pointed out by Weillbacher *et al.* (2000), a possible descendent of such objects at the tips of tidal tails is tidal dwarf galaxies. Another tendency is that bright knots are less frequently seen in single nucleus ULIRGs, compared with multiple/double mergers. We plan to study the properties of these bright knots and investigate their formation mechanisms and evolutionary fates in a future work.

### 5.1. Multiple nuclei ULIRGs

Table 3 gives the information on each nucleus for all the 17 multiple mergers, while the *HST* *I*-band images, surface plots and contour plots are shown in Figs. 1-17 (arranged from left to right, respectively). We put plus marks on each image to indicate the positions of putative nuclei, and the orientation of the image is indicated by the headed north arrow and the unheaded east arrow. Since pixel spacings are not always the same for the two axes, the north and east directions may sometimes be oblique. The orientation of each contour plot is selected to be the same as the snapshot image for direct comparison. For the three-dimensional surface plot, we rotate it along both horizontal and vertical viewing directions until it renders the best sight to view each nucleus clearly. In addition, for each multiple merger candidate, the snapshot image and the contour plot both contain distance scale rulers, and the scale of the surface plot is selected to be the same as that of the contour plot. For the 17 multiple merger systems, the morphologies, the relative positions and numbers of putative nuclei as well as knots are very different. We give a description of each target in turn.

**IR00161–0850** This galaxy is mainly composed of two parts separated by 4.3 kpc. The northeastern part contains a single nucleus, while the southwestern part consists of two close

nuclei with a projected separation of only 570 pc. Bright knots of the system preferentially distribute to the southwest of each nucleus. There is a 45 kpc tidal tail starting from the northeastern nucleus and curving to the south. In addition, the contour plot of IR00161–0850 presents distinct arm structures connected to both parts of the system. These structures may be remnants of progenitor spiral arms which have not been completely destroyed by the merging process.

**IR02364–4751** The western part of IR02364–4751 contains the brightest nucleus of the system, while the eastern part is composed of two close nuclei separated by 540 pc. The projected distance between the two parts is about 2.6 kpc and several bright knots can clearly be seen between them. A 50 kpc tidal tail starts at the eastern nucleus pair and curves from the east to the west. A faint plume structure can also be seen starting from the western nucleus and stretching to the southwest. A possible evolutionary scenario is that two spirals merge first and produce the long tail we see; before they finally evolve into a single object, a third galaxy approaches from their western side, which makes up a system with three putative nuclei.

**IR03538–6432** The morphology of this galaxy is like that of Mrk 273. A very long tidal tail of nearly 40 kpc starts from the central star-like object and stretches from the northeast to the southwest. Surface and contour plots of the target clearly show that the central object is in fact composed of three closely separated nuclei all brighter than  $-20.5$  mag in the  $I$ -band. According to the spectral information, the central active galactic nuclei (AGN) phenomenon is triggered in this target. The three progenitor galaxies of this system are likely to have begun merging almost simultaneously.

**IR04384–4848** The morphology of this galaxy is asymmetric and complex. Three bright putative nuclei of about  $-19.0$  mag exist in the system, with a roughly linear distribution. The projected separation is about 800 pc (between the center and western nucleus) and 1.1 kpc (between the center and eastern nucleus). Two plume structures are detectable in the system, with the western one being 9 kpc long and the northeastern one 5 kpc long. Several bright knots distribute just along these two plumes. Furthermore, two much fainter plumes can also be seen from the snapshot image, stretching to the southwest and east, respectively. These fainter plumes are also much longer, the southwestern one is nearly 28 kpc long while the eastern one is about 23 kpc long.

**IR13539+2920** From the snapshot image, this galaxy consists of two parts located to the northwest and southeast, respectively. The projected separation between these two parts is about 6.5 kpc. The southeastern component embeds two close nuclei separated by 2.2 kpc, and a tidal plume starts here stretching as far as 10 kpc. This gives further support to the merger origin of the southeastern component.

**IR14060+2919** This galaxy is a system with peculiar morphology. The three putative nuclei we identified approximately distribute along a line. The central nucleus is 0.5 kpc and 1 kpc

away from the eastern and western nucleus, respectively. In the global environment, the three closely separated nuclei reside at the southern edge of a tidal ring with 11 kpc diameter, and several bright knots are scattered along the ring perimeter. These putative nuclei are also connected with a 14 kpc tail curving from the east to the west. A possible explanation of this peculiar morphology is that two galaxies interact to produce a tidal tail, and before their bulges finally merge together, a third galaxy impact on them perpendicular to their disk planes, which results in the ring structure we see now.

**IR14202+2615** This system contains two main parts separated by about 15 kpc, and a material stream can be detected connecting these two parts. The center of the western part is a compact nucleus with *I*-band absolute magnitude about  $-19.3$  mag. Two distinct spiral arms extend from it and stretch to the north and south, respectively. Along the two arms there are several bright and compact knots, two of which are almost as bright as  $-18.0$  mag. However, since these very bright clumps reside at the tip of the southern spiral arm, they are more likely to be progenitors of tidal dwarf galaxies, and hence are not identified as putative nuclei in our work (see Sec. 4). In addition, two other nuclei brighter than  $-19.0$  mag are located along the two spiral arms.

**IR14575+3256** Surface and contour plots of IR14575+3256 show clearly that there are three distinct putative nuclei in the system. A close pair separated by 1 kpc is located to the east, while a fainter nucleus is located to the west. The projected separation between these two parts is about 2.4 kpc. Although its three nuclei are closely distributed, IR14575+3256 only presents moderate interacting features. A 10 kpc arm starts from the two eastern nuclei and curves to the southwest, while a 6 kpc arm starts from the western nucleus and curves to the north. Several bright knots preferentially distribute along these two arms as well as around the two eastern nuclei.

**IR16007+3743** This is an object with very peculiar morphology which may be hard to explain as a pair merger product. The snapshot image shows a round center component, which is connected with two other bar-like structures to the northwest and southwest, respectively. Each of these three components encompasses a bright nucleus. In fact, there are two closely separated clumps in the southwestern *bar* which are both brighter than  $-18.0$  mag. However, due to their contour shapes, these two clumps appear to be a single nucleus split by a foreground dust lane (as in the case of IR05189–2524, see Surace *et al.* 1998). Hence we conservatively take them as a single object, and the  $M_I$  value listed in Table 3 is the combined magnitude of these two objects. A 11 kpc tidal plume starts from the central component and curves to the south. In addition, another tidal tail as long as 19 kpc is also detectable connected to the northwestern *bar* and stretches from the west to the east.

**IR18580+6527** The morphology of this galaxy is rather complicated. A strong tidal ring can be seen from the *HST* snapshot image and its diameter is about 20 kpc. The main part of this galaxy is located at the northern edge of the ring perimeter. The galaxy is clearly composed

of four compact nuclei, as shown in the surface and contour plots. These four putative nuclei are very bright, each with *I*-band absolute magnitude around  $-20.0$  mag. 6 kpc away to the north of these four nuclei is located the fifth nucleus of the system, and a 12 kpc plume structure just starts here stretching from the south to the north.

**IR20037–1547** This is an example of a QSO hosted in an interacting galaxy system. Besides the central brightest nucleus with *I*-band absolute magnitude of nearly  $-23.0$ , there exist another two bright nuclei which are separated by 1.1 kpc and located to the southeast. A distinct ring structure with a diameter of about 19 kpc locates to the north of the system. This galaxy resembles 3C 48 and IR04505–2958 in morphology and it provides us with direct evidence that the AGN phenomenon can be triggered by galaxy merging.

**IR20100–4156** From the HST morphology, this is clearly a merging pair with two parts to the north and south, respectively. These two parts are separated by 6 kpc and some bright knots can be seen located around each part. Both the northern and southern parts consist of two distinct nuclei, separated by 1.6 kpc and 3.1 kpc, respectively. In addition, tidal plume structures can be seen connected to these two parts. From its morphological features, it is likely that the progenitor of this system is a group of four galaxies; each pair of galaxies merge first, while the whole system begins its encounter before each pair finishes its own merging process.

**IR20253–3757** From the *HST* snapshot image, this galaxy is composed of two main parts to the south and north, respectively. The projected separation between these two parts is about 5 kpc. The southern part encompasses a single nucleus, while the northern part has four close nuclei in a roughly linear distribution, whose high *I*-band luminosities suggest that they are not very likely to be star-forming knots. Only weak interacting features are detectable in the system. A faint plume stretching from the south to the north is connected with the four northern nuclei. In addition, another faint tidal ring is detectable to the east of the main body.

**IR21130–4446** This ULIRG has a rather peculiar morphology which consists of two parts from the snapshot image. The northeastern part has a ring-like structure with a diameter of more than 8 kpc. Four separate nuclei are concentrated at its south side, while a number of bright knots can also be clearly seen along the ring. The southwestern part of this system consists of two close nuclei separated by 600 pc and their connecting line is perpendicular to the northeastern ring plane. In addition, there exists a tidal bridge connecting these two parts.

**IR22206–2715** This is a three nuclei ULIRG with very peculiar morphology. The bright object located in the center is composed of two close nuclei separated by 1.2 kpc, while another much fainter nucleus resides to their northeast. A clear tidal bridge can be seen connecting these two parts, and several bright knots are distributed just along the bridge. Two plume structures of length 6 kpc and 18 kpc start from the central nucleus pair and curve in

opposite directions. In addition, connected to the northeastern nucleus, there is a 25 kpc tidal tail stretching directly from the east to the west.

**IR22491–1808** This system contains three putative nuclei with very different luminosities. The one located at the center has  $I$ -band luminosity as high as  $2.6 \times 10^9 L_{\odot}$ . The nucleus located 1.2 kpc to the southeast of the central bright nucleus and the one 2.4 kpc to the west are much fainter. In addition, bright star-forming knots of the system are preferentially distributed around the western nucleus. A multiple merger scenario of this system is also supported by its complex morphology with a 11 kpc tidal tail and two other plume structures.

**IR23515–2421** From the snapshot image, this is a galaxy with a relatively simple and regular morphology. A distinct tidal tail about 19 kpc long starts from the central bright object and stretches from the northwest to the southeast. The central object is in fact composed of three close nuclei all brighter than  $-19.5$  mag, and around them there are several bright star-forming knots of the system. The three progenitor galaxies of this system are likely to have begun to merge almost simultaneously.

As described above, all of the targets listed in Table 3 encompass at least three putative nuclei and most of them clearly show signs of strong interaction activities. Such large scale tidal features coined as *tidal traumas* (Barnes & Hernquist 1992) include tails, bridges, rings, plumes, etc. In some systems with very peculiar morphologies, different types of tidal features may co-exist, such as several tails or plumes (e.g., IR22206–2715 in Fig. 15). Borne *et al.* (2000) suggested that merging pairs of spirals alone can not account for all the dynamical diversities of ULIRGs, and numerical simulations also support that such complex structures tend to appear in multiple merger systems (Barnes & Hernquist 1996).

## 5.2. $I$ -band magnitudes of putative nuclei and spectral types

The  $I$ -band magnitude distributions of putative nuclei for the whole sample and the three different categories are presented in Figs. 18a-d, respectively. The faint side cutoff in Figs. 18b and 18c (multiple and double nuclei galaxies) is set by our criterion. In Fig. 18d (single nucleus galaxies), the faint side cutoff is at  $-18.0$  mag. This might be due to the merger-induced formation of massive and bright bulges in these systems. On the other hand, there exists a distinct high luminosity tail above  $M_I = -21.0$  in Fig. 18d. This corresponds to a Seyfert 1/QSO excess in single nucleus ULIRGs, since most nuclei brighter than  $-21$  mag (9 out of 13 with available spectra) belong to galaxies with Seyfert 1/QSO spectra (see Tables 3, 4 and 5). In addition, Seyfert 1/QSO nuclei can occasionally be found in multiple/double mergers (e.g., IR20037–1547 and IR00204+1029), and there is either likelihood that these bright nuclei are primordial objects before merger or in fact evolutionary descendents of previous merging steps.

The magnitude distributions of multiple/double mergers and single nucleus galaxies give a

median  $I$ -band magnitude of  $-19.3$  ( $2.3 \times 10^9 L_\odot$ ) and  $-20.1$  ( $4.7 \times 10^9 L_\odot$ ), respectively. The high median luminosity for the single nucleus category is partly due to the merger-induced formation of massive, bright bulges, and partly due to the triggering of active galactic nuclei (AGN) phenomenon in a substantial fraction of merger remnants, as mentioned above. In addition, these three categories do not show much difference in the  $M_I$  distribution width. Although magnitude distributions of multiple and double mergers do not present much differences, it is obvious from the comparison of Figs. 18b and 18c that bright nuclei (i.e., from  $-19.5$  to  $-20.5$  mag) tend to appear more often in double nuclei systems (nearly twice as often than in multiple mergers). This gives some hints to a possible evolutionary sequence from galaxy groups to merger remnants with a single nucleus, along which the double nuclei systems remain as intermediate products (M→D→S sequence).

To check this M→D→S merger sequence, we calculate the luminosity ratio of each nucleus to the brightest one in the same target. Our results show that nearly 40% of the double merger ULIRGs contain two nuclei with mass ratio more than 3:1 (assuming a constant mass-to-light ratio for bulge). Although spiral galaxies might possess rather different bulge-to-disk mass ratios, it cannot be ruled out that a substantial fraction of putative nuclei in pair merger are likely to be merger remnants of previous galaxy encounters, since ULIRGs are postulated to arise from mergers of two comparably massive gas-rich spiral galaxies (e.g., Mihos 1999). This gives further support to a possible M→D→S evolutionary sequence.

Further investigation based on the optical spectra available in the literature (Lawrence *et al.* 1999; Veilleux *et al.* 1999) as well as the information from NED <sup>1</sup> and our observations shows that about 64% (7/11) Seyfert 1/QSO in this *HST* snapshot imaging survey sample belong to galaxies with a single nucleus. This gives an important hint that the Seyfert 1/QSO phenomenon tend to appear at the final stage of galaxy interactions/mergers when separate nuclei have merged together. Table 6 gives the detailed statistics of different spectral types for the three categories. It shows that the proportions of H II region-like spectra are 64% (9/14), 35% (8/21) and 20% (5/25) for multiple, double and single nucleus/nuclei galaxies, respectively. While the AGN proportions for these three categories are 36% (5/14), 65% (13/21) and 80% (20/25). This clear trend of gradually changing proportions of different spectral types suggests that the M→D→S sequence is also one with changing energetics: from starburst-dominated to central AGN-dominated. Of course, it should be mentioned that the H II-like spectra in some objects may be due to the super star clusters rather than the identified putative nuclei, which is consistent with the fact that the images of these targets are distributed by knotty structures in their circumnuclear regions (e.g., IR14202+2615 and IR18580+6527 ).

---

<sup>1</sup>The NASA/IPAC *Extragalactic Database* (NED) is operated by the Jet Propulsion Laboratory, California Institute of Technology, under contract with the National Aeronautics and Space Administration.

### 5.3. Nuclear separations and tail lengths

Tables 3 and 4 list the projected nuclear separations for multiple and double nuclei ULIRGs. We present the corresponding distributions in Fig. 19a. Given the *HST* WFPC2 resolution limit, our measurements cannot probe separations below several hundred parsecs, except for some low redshift galaxies. At the maximum redshift in the sample,  $z = 0.35$ , our measurements can only probe nuclear separations larger than 1.5 kpc. Therefore the distribution of nuclear separations less than this value is incomplete. This incompleteness is particularly serious at separations below 0.5 kpc, since very few targets in this sample are at low redshift (i.e., less than 20% with redshift smaller than 0.1). This is shown by the sharp decrease below 500 pc in Fig. 19a. We also give the same distribution based on results from the literature (Surace *et al.* 1999; Evans 1999; Rigopoulou *et al.* 1999; Murphy *et al.* 1996; Clements *et al.* 1996) in Fig. 19(b) for comparison. One significant feature of our results is that there is a high fraction (3/4) of nucleus pairs with projected separations less than 5 kpc, which is much higher than the result from the literature (1/3). The reason for this large difference is mostly due to the low resolution limit of ground-based observations in previous works. This result supports that systems at late merging stage preferentially host ULIRG galaxies (Mihos 1999).

Fig. 20 displays the correlation between nuclear separations and tail lengths. Most of the data points are distributed in the lower left corner of the plot. However, considering that both the minimum separations and tail lengths applied here are projected values, the distribution profile of data points is more instructive. Fig. 20 shows a weak trend of smaller nuclear separations coupled to longer tidal tails. Simple qualitative analysis suggests a picture that when galaxies first encounter at a relatively large distance, their mutual tidal field is not strong enough to produce long tail structures; and when they are drawn closer as the merging process proceeds, disk stars in each galaxy are catapulted farther out and tidal tails continue to lengthen. This picture is consistent with numerical simulations (e.g., Toomre & Toomre 1972; Wright 1972). However, there do exist several examples with both long tails and large nuclear separations (e.g., IR21547–5823). This might imply that at least one nucleus in such systems is in fact an evolutionary descendent of a previous merging process, or merely that the resolution limit of *HST* prevents us from probing fine structures at its very center. Considering this, the multiple merger fractions we determined at the beginning of Sec. 5 might be an under-estimate of the true fraction. In addition, relatively short tail structures can occasionally be found in single nucleus ULIRGs. This further strengthens the case that these systems are merger remnants of previous galaxy encounters. Of course, our measurements of tail length carry an obvious bias: the observable tidal tails at a given surface brightness in distant galaxies tend to be shorter than their nearby counterparts even if they have the same physical lengths, due to the  $(1+z)^4$  surface brightness dimming. However, since the sample targets do not cover a wide range of redshifts (0.04→0.35), this effect should not influence our statistical results significantly.

## 6. Discussion and summary

### 6.1. Multiple merger fraction

Based on our quantitative criterion as well as morphological features, we obtain the fractions for multiple, double and single nucleus/nuclei ULIRGs as 18%, 39% and 43%, respectively. A question is why there is no report of multiple merger cases in other sample studies on ULIRGs, e.g., in the sample of Surace *et al.* (1998). To test the consistency between these two results, we directly apply an upper mass limit of  $10^9 M_\odot$  on their results of ULIRG knots as well as putative nuclei, and find that two targets in their sample (IR12071–0444 and IR15206+3342) should be classified as multiple mergers, namely, there are at least three clumps too massive to be explained as star cluster associations in each of these two targets. Considering this, the fraction of multiple nuclei ULIRGs in Surace’s sample is 22%, very close to our result of 18%. The main reason why Surace *et al.* (1998) did not choose these objects as multiple merger systems might be that only the one or two brightest clumps in their sample were believed to plausibly represent putative nuclei. This means the pair merger origin was considered to be the only evolutionary picture for ULIRGs. This assumption may sometimes give rise to some inconsistencies or ambiguities. This is especially true in the case of IR12071–0444. For this system, there are three bright objects that have comparable masses (several times  $10^9 M_\odot$ ), but only one of them was selected as a putative nucleus. Furthermore, this identified nucleus also possesses  $M_B$ ,  $M_I$  and  $B - I$  values just between those of the other two bright clumps (see Table 2 of Surace *et al.* 1998). This means that at least this putative nucleus does not show distinguished features compared with some other clumps in the same target. Thus it is possible that any of the three brightest clumps in IR12071–0444 represent putative nuclei. On the other hand, in our work, the putative nuclei were identified independent of the evolutionary origin for ULIRGs, in order to check the possibility of the multiple merger scenario proposed by some researchers.

Based on the same sample, the multiple merger candidates selected by Borne *et al.* (2000) include 9 ULIRGs classified as multiple nuclei galaxies and 8 ULIRGs classified as interacting groups (three multiple mergers in Borne’s classification are absent from our subsample, and are therefore not discussed here). The *HST* snapshot imaging survey sample does include a fraction of ULIRGs which are very likely to be located within galaxy groups from their images, since there are several bright or dwarf galaxies surrounding them. However, we did not consider them as multiple merger systems except when the central target contains at least three putative nuclei or is connected with some of its companions by obvious interacting signatures. This is because further redshift observations need to be performed for confirmation. These group candidates include IR00335–2732, IR01031–2255, IR06268+3509, IR13342+3932 and IR22546–2637. In fact, we have carried out some spectroscopic observations using the 2.16 m telescope at the Xinglong Station of Beijing Astronomical Observatory and identified several luminous/ultraluminous IRAS galaxies located in galaxy groups (Zou *et al.* 1995; Wu *et al.* 1998). However, for two multi-merger (group) candidates in Table 1 (IR02459–0233 and IR12202+1646), neither of them belong to

an interacting group since the surrounding galaxies are either foreground or background objects (Zheng *et al.* 1999). Considering that the evolutionary sequence from galaxy groups to ULIRGs and then to ellipticals is attractive from both theoretical and observational points of view, further detailed multi-wavelength observations on these group candidates have been scheduled.

As for the remaining 12 multiple mergers in Borne’s classifications, six of them are consistent with our classifications (IR13539+2920, IR16007+3743, IR18580+6527, IR20100–4156, IR20253–3757 and IR23515–2421). We carefully examined the six discrepant targets, of which five of them contain only one or two clumps brighter than  $-17.0$  mag in the  $I$ -band. Therefore they are classified as single or double nucleus/nuclei ULIRGs. The case for IR14337–4134 is somewhat confusing. This target seems to reside in a group composed of several bright galaxies as well as star-like objects, of which the biggest galaxy indeed contains three obvious nuclei. However, the star-like object located in the center is the nearest target to the IRAS position. In addition, the QDOT redshift survey (Lawrence *et al.* 1999) reveals that its optical spectral type is Seyfert 1 and the calculation of far-infrared luminosity for IR14337–4134 is also based on the redshift of this Seyfert galaxy. Considering this, Borne *et al.* (2000) may have identified the wrong target on the WFPC2 snapshot image. Putting aside IR14337–4134, we suggest that the remaining five multiple mergers in Borne’s identification which are absent from our results are due to different selection criteria involved. Borne *et al.* (2000) identified several targets with very complex tidal features to be multiple merger cases with no regard for the exact numbers of their observable nuclei. Although it is likely that a very complex morphology does point to a possible multiple merger origin, we identify multiple mergers simply based on the exact number of clumps brighter than  $-17.0$  mag, because any tight correlation between morphologies and nucleus numbers needs to be verified by further numerical simulations of merging processes.

## 6.2. Some hints for merging dynamics

1. From luminosity distributions in Sec. 5.2, it is obvious that putative nuclei in single nucleus ULIRGs tend to be more luminous than those in multiple/double mergers. Statistical studies on available spectral information also reveal that there is a Seyfert 1/QSO excess in the single nucleus category. Therefore, our results strongly support the argument of Kauffmann & Haehnelt (2000) that bulge and supermassive black holes may both grow in galaxy merging. And our results also give some hints to a possible close relation between central black holes and the bulges of their host galaxies. (Gebhardt *et al.* 2000).
2. Although only a small fraction of snapshot images are given in this paper, there is no doubt from morphological comments in Tables 3, 4 and 5 that most ULIRGs with single nuclei have weak interacting signatures (in many cases, only weak plume structures are detectable). On the other hand, peculiar morphologies frequently emerge in double/multiple nuclei ULIRGs, such as long tidal tails and distinct ring structures. This indicates that strong interacting features always thin out at final merging phase, which is consistent with results

from numerical simulations (e.g., Barnes & Hernquist 1996).

3. From the detailed descriptions in Sec. 5.1, we can see that multiple merger processes may be very complicated and the morphologies of their intermediate products may be very diverse. This indicates that the evolutionary history of interactions/mergers in galaxy groups must vary due to different initial conditions. When a group of galaxies begins to merge, the central massive spiral may swallow its satellite galaxies one by one; on the other hand, merging processes may also happen between several galaxy pairs or among sub-groups simultaneously, then these separate parts start a second merging step. Major mergers between comparably massive spirals alone cannot account for the dynamical diversity of the ULIRG population (Borne *et al.* 2000).

We would like to express our gratitude to the staff members at the Beijing Astronomical Center, especially W.-P. Lin and H. Wu, for generous help in data reduction. We also wish to thank Z. Zheng and the anonymous referee for useful comments and suggestions, which improved the paper. We are also grateful to Martin Smith for a careful reading of the text. This research was based on observations obtained with the NASA/ESA *Hubble Space Telescope* through the Space Telescope Science Institute, Astronomy, Inc., under NASA contract NAS5-26555. This project was supported by the NSFC and NKBRSF G19990754.

## REFERENCES

- Ashman, K.M., & Zepf, S.E. 1992, ApJ, 384, 50
- Barnes, J.E. 1984, MNRAS, 208, 873
- Barnes, J.E. 1985, MNRAS, 215, 517
- Barnes, J.E. 1989, Nature, 338, 123
- Barnes, J.E. 1992, ApJ, 393, 484
- Barnes, J.E. 1999, Galaxy Dynamics, ASP Conference Series, 182, 463
- Barnes, J.E., & Hernquist, L. 1992, ARA&A, 30, 705
- Barnes, J.E., & Hernquist, L. 1996, ApJ, 471, 115
- Bendo, G.J., & Barnes, J.E. 2000. MNRAS, 316, 315
- Borne, K.D., Bushouse, H., Colina, L., Lucas, R.A., Baker, A., *et al.* 1999a, Astrophysics with Infrared Surveys: A Prelude to SIRTf, ASP Conference Series, 177, 167
- Borne, K.D., Bushouse, H., Colina, L., Lucas, R.A., Baker, A., *et al.* 1999b, Ap&SS, 266, 137
- Borne, K.D., Bushouse, H., Lucas, R.A., & Colina, L. 2000, ApJ, 529, L77
- Burnstein, D. 1987, in Nearly Normal Galaxies, edited by S. Faber(Springer, New York), p. 47
- Clements, D.L., Sutherland, W.J., McMahon, R.G., & Saunders, W. 1996, MNRAS, 279, 477
- de Grijs, R., O’Connell, R.W., & Gallagher, J.S. 1999, American Astronomical Society Meeting 195, #47.11
- Duc P.-A., & Mirabel, I.F. 1997, in IAU symposium 186, Galaxy Interactions at Low and High Redshift, p.61
- Elmegreen, B.G., & Efremov, Y.N. 1997, ApJ, 480, 235
- Evans, A.S. 1999, Ap&SS, 266, 73
- Farouki, R.T., & Shapiro, S.L. 1982, ApJ, 259, 103
- Fellhauer, M., & Kroupa, P. 2000, Massive Stellar Clusters, Proceedings of the international workshop, p.241
- Gallagher, J.S., Homeier, N.L., & Conselice, C.J. 2000, Massive Stellar Clusters, Proceedings of the international workshop, p.258
- Gebhardt, K., Bender, R., Bower, G., Dressler, A., Faber, S.M., *et al.* 2000, ApJ, 539, 13

- Hernquist, L. 1992, ApJ, 400, 460
- Heyl, J., Hernquist, L., & Spergel, D.N. 1994, ApJ, 427, 165
- Holtzman, J.A., Faber, S.M., Groth, E.J., Hunter, D.A., Baum, W.A., *et al.* 1992, AJ, 103, 691
- Holtzman, J., Hester, J., Casertano, S., Trauger, J.T., Watson, A.M., *et al.* 1995, PASP, 107, 156
- Hutchings, J.B. 1995, AJ, 111, 712
- Kauffmann, G. & Haehnelt, M. 2000, MNRAS, 331, 576
- Kumai, Y., Basu, B., & Fujimoto, M. 1993, ApJ, 404, 144
- Lauer, T.R., 1985, ApJ, 292, 104
- Lawrence, A., Rowan-Robinson, M., Ellis, R.S., Frenk, C.S., Efstathiou, G., *et al.* 1999, MNRAS, 308, 897
- Leech, K.J., Rowan-Robinson, M., Lawrence, A., & Hughes, J.D. 1994, MNRAS, 267, 253
- Lin, D.N.C., Pringle, J.E. & Rees, M.J. 1988, ApJ, 328, 103
- Lipari, S., Díaz, R., Taniguchi, Y., Terlevich, R., Dottori, H., *et al.* 1999, AJ, 120, 645
- Lutz, D. 1991, A&A, 245, 31
- Mamon, G.A. 1987, ApJ, 321, 622
- Melnick, J., & Mirabel, I.F. 1990, A&A, 231, L19
- Meurer, G. 1995, Nature, 375, 742
- Meurer, G., Heckman, T., Leitherer, C., Kinney, A., Robert, C., *et al.* 1995, ApJ, 110, 2665
- Mihos, J.C., & Hernquist, L. 1994, ApJ, 431, L9
- Mihos, J.C. 1999, Ap&SS, 266, 195
- Murphy, T.W., Armus, Jr.L., Matthews, K., Soifer, B.T., Mazzarella, J.M., *et al.* 1996, AJ, 111, 1025
- Negroponte, J. & White, S.D. 1983, MNRAS, 205, 1009
- Noguchi, M. 1999, ApJ, 514, 77
- Rigopoulou, D., Spoon, H.W.W., Genzel, R., Lutz, D., Moorwood, A.F.M. *et al.* 1999, AJ, 118, 2625
- Sakamoto, K., Scoville, N.Z., Yun, M.S., Crosas, M., Genzel, R., *et al.* 1999, ApJ, 514, 68

- Sanders, D.B., & Mirabel, I.F. 1996, *ARA&A*, 34, 749
- Sanders, D.B., Soifer, B.T., Elias, J.H., Madore, B.F., Matthews, K., *et al.* 1988a, *ApJ*, 325, 74
- Sanders, D.B., Soifer, B.T., Elias, J.H., Neugebauer, G., & Matthews, K. 1988b, *ApJ*, 328, L35
- Sanders, D.B., Surace, J.A., & Ishida, C.M. 1999, in *IAU symposium 186, Galaxy Interactions at Low and High Redshift*, p.289
- Scoville, N.Z., Evans, A.S., Thompson, R., Rieke, M., Hines, D.C., *et al.* 2000, *AJ*, 119, 991
- Schweizer, F. 1987, in *Nearly Normal Galaxies*, edited by S. Faber (Springer, New York), p. 18
- Schweizer, F. 1989, *Nature*, 338, 119
- Shioya, Y., Taniguchi, Y., & Trentham, N. 2000, astro-ph/0008312, Accepted for publication in *MNRAS*
- Springel, V., & White, S.D.M. 1998, *MNRAS*, 307, 162
- Surace, J.A., Sanders, D.B., Vacca, W.D., Veilleux, S., & Mazzarella, J.M. 1998, *ApJ*, 492, 116
- Surace, J.A., & Sanders, D.B. 1999, *ApJ*, 512, 162
- Surace, J.A., Sanders, D.B. & Evans, A.S. 1999, *ApJ*, 529, 170
- Taniguchi, Y., & Shioya, Y. 1998, *ApJ*, 501, L167
- Taniguchi, Y., Trentham N. & Shioya, Y. 1998, *ApJ*, 504, L79
- Toomre, A., & Toomre, J. 1972, *ApJ*, 178, 623
- Veilleux, S., Kim, D.-C., & Sanders, D.B. 1999, *ApJ*, 522, 113
- Walker, I.R., Mihos, J.C. & Hernquist, L. 1996, *ApJ*, 460, 121
- Weil. M.L., & Hernquist, L. 1996, *ApJ*, 460, 101
- Weilbacher, P.M., Duc, P.-A., Fritze-v.Alvensleben, U., Martin, P. & Fricke, K.J. 2000, *A&A*, 358, 819
- White, S.D.M. 1978, *MNRAS*, 184, 185
- Whitmore, B., & Schweizer, F. 1995, *AJ*, 109, 960
- Wright, A.E. 1972, *MNRAS*, 157, 309
- Wu, H., Zou, Z.-L., Xia, X.-Y., & Deng, Z.-G. 1998, *A&AS*, 132, 181
- Zepf, S.E., & Ashman, K.M. 1993, *MNRAS*, 264, 611

Zheng, Z., Wu, H., Mao, S., Xia, X.-Y., Deng, Z.-G, *et al.* 1999, A&A, 349, 735

Zou, Z.-L., Xia, X.-Y., Deng, Z.-G., & Wu, H. 1995, A&A, 304, 369

Table 1. Sample of ULIRGs observed with WFPC2 of HST.

No.	Target name	RA(2000)	Dec(2000)	Redshift <sup>a</sup>	$\log \frac{L_{\text{IR}}}{L_{\odot}}$ <sup>b</sup>	Classification
uc7	IR00060–1543	00:08:38	–15:26:52	0.195	12.0	Double
uc9	IR00105–0139	00:13:04	–01:23:05	0.164	11.9	Double
u33	IR00150+4937	00:17:45	49:54:11	0.149	11.9	Double
ud0	IR00161–0850	00:18:43	–08:33:36	0.109	11.8	Multiple
u57	IR00204+1029	00:23:22	10:46:22	0.230*	<12.3	Double
u59	IR00275–2859	00:30:04	–28:42:26	0.280	12.4	Single
ud2	IR00335–2732	00:36:01	–27:15:35	0.069	11.8	Single
u60	IR00461–0728	00:48:39	–07:12:19	0.243	12.2	Double
u01	IR00509+1225	00:53:35	12:41:36	0.062	11.5	Single
ud4	IR00589–0352	01:01:31	–03:36:28	0.176	12.0	Double
ud5	IR01031–2255	01:05:37	–22:39:18	0.186*	11.9	Single
u65	IR02054+0835	02:08:07	08:50:04	0.345	12.5	Single
u02	IR02364–4751	02:38:13	–47:38:12	0.098	12.0	Multiple
uf0	IR02459–0233	02:48:28	–02:21:35	0.180	12.0	Double
u68	IR03538–6432	03:54:25	–64:23:45	0.300	12.6	Multiple
ub0	IR04024–8303	03:57:11	–82:55:16	0.140*	11.8	Single
u69	IR04384–4848	04:39:51	–48:43:15	0.203	12.2	Multiple
u70	IR04413+2608	04:44:31	26:14:10	0.171	12.1	Single
u71	IR05120–4811	05:13:24	–48:07:58	0.162	12.0	Double
ub1	IR05116+7745	05:19:12	77:48:12	0.158	11.9	Single
u72	IR05233–2334	05:25:27	–23:32:08	0.171	11.9	Single
u03	IR06035–7102	06:02:54	–71:03:09	0.079	12.0	Double
u04	IR06206–6315	06:21:01	–63:17:23	0.091	12.1	Double
u73	IR06268+3509	06:30:13	35:07:50	0.170	12.0	Double
u74	IR06361–6217	06:36:36	–62:20:32	0.159	12.2	Single
ub4	IR06487+2208	06:51:46	22:04:30	0.144	12.2	Double
u75	IR06561+1902	06:59:06	18:58:21	0.188	12.1	Double
ub5	IR07246+6125	07:29:12	61:18:53	0.138	11.7	Single
u76	IR07381+3215	07:41:23	32:08:09	0.170	11.9	Single
u77	IR08201+2801	08:23:13	27:51:39	0.167	12.1	Double
ub7	IR08344+5105	08:38:04	50:55:09	0.097	11.8	Double
ub8	IR08509–1504	08:53:16	–15:15:48	0.135	12.0	Single
ub9	IR09039+0503	09:06:34	04:51:28	0.124	11.9	Double
u05	IR09320+6134	09:35:52	61:21:11	0.040	11.9	Single
u49	IR09425+1751	09:45:21	17:37:54	0.128	11.7	Single
u50	IR09427+1929	09:45:29	19:15:50	0.150*	11.7	Single
u78	IR10026+4347	10:05:42	43:32:39	0.177	11.9	Single
uc2	IR10122+4943	10:15:21	49:28:19	0.154*	11.9	Single
u79	IR10558+3845	10:58:39	38:29:06	0.207	12.1	Single
u80	IR10579+0438	11:00:34	04:22:08	0.173	11.9	Single
uc3	IR11087+5351	11:11:37	53:34:57	0.143	11.8	Double
u06	IR11095–0238	11:12:03	–02:54:23	0.105	12.1	Double
u81	IR12108+3157	12:13:20	31:40:53	0.207	12.2	Single
u07	IR12112+0305	12:13:46	02:48:41	0.072	12.2	Double
u82	IR12202+1646	12:22:47	16:29:45	0.181	12.1	Single

Table 1—Continued

No.	Target name	RA(2000)	Dec(2000)	Redshift <sup>a</sup>	$\log \frac{L_{\text{fir}}}{L_{\odot}}$ <sup>b</sup>	Classification
u34	IR12490–1009	12:51:41	–10:25:26	0.100	11.8	Double
u24	IR13144+2356	13:16:54	23:40:46	0.138	11.8	Single
u25	IR13342+3932	13:36:24	39:17:29	0.180	12.2	Single
u83	IR13352+6402	13:36:51	63:47:04	0.237	12.4	Double
u08	IR13428+5608	13:44:42	55:53:11	0.038	12.0	Double
u26	IR13442+2321	13:46:39	23:06:21	0.142	12.1	Single
u36	IR13469+5833	13:48:40	58:18:52	0.158	12.1	Double
u27	IR13539+2920	13:56:10	29:05:36	0.109	11.9	Multiple
u28	IR14060+2919	14:08:19	29:04:46	0.117	11.9	Multiple
u29	IR14170+4545	14:18:59	45:32:12	0.151	11.8	Single
u30	IR14202+2615	14:22:31	26:02:06	0.159	12.1	Multiple
u31	IR14312+2825	14:33:28	28:11:59	0.175	12.0	Double
u85	IR14337–4134	14:36:58	–41:47:11	0.182	12.0	Single
u09	IR14348–1447	14:37:38	–15:00:23	0.082	12.2	Double
u10	IR14378–3651	14:40:59	–37:04:33	0.068	12.0	Single
u32	IR14575+3256	14:59:37	32:44:58	0.114	11.8	Multiple
u38	IR15413–0959	15:44:05	–10:09:00	0.160	11.8	Single
u54	IR16007+3743	16:02:33	37:34:53	0.185*	11.6	Multiple
u86	IR16159–0402	16:18:37	–04:09:44	0.213	12.2	Single
u39	IR16455+4553	16:46:59	45:48:23	0.191	12.2	Single
u41	IR16541+5301	16:55:20	52:56:36	0.194	12.1	Double
u42	IR17179+5444	17:18:54	54:41:49	0.148	12.1	Single
u87	IR17431–5157	17:47:10	–51:58:44	0.175	12.0	Single
u88	IR17463+5806	17:47:05	58:05:21	0.310	12.4	Single
u44	IR18580+6527	18:58:14	65:31:29	0.177	12.0	Multiple
u14	IR19254–7245	19:31:22	–72:39:20	0.061	11.8	Double
u15	IR19297–0406	19:32:22	–04:00:01	0.086*	12.2	Single
uc5	IR19561–4756	19:59:49	–47:48:17	0.139	11.9	Double
u90	IR20037–1547	20:06:31	–15:39:06	0.192	12.4	Multiple
u16	IR20087–0308	20:11:24	–02:59:52	0.106	12.3	Multiple
u17	IR20100–4156	20:13:30	–41:47:34	0.130	12.5	Multiple
u91	IR20109–3003	20:14:06	–29:53:51	0.143	11.8	Single
u92	IR20176–4756	20:21:11	–47:47:07	0.178	12.1	Single
u93	IR20253–3757	20:28:38	–37:47:09	0.180	12.0	Multiple
u94	IR20314–1919	20:34:18	–19:09:12	0.153	11.9	Double
u18	IR20414–1651	20:44:18	–16:40:16	0.088	12.1	Single
u95	IR20507–5412	20:54:26	–54:01:17	0.228	12.2	Double
u19	IR20551–4250	20:58:27	–42:39:03	0.043	11.9	Double
u20	IR21130–4446	21:16:19	–44:33:40	0.093	12.0	Multiple
u96	IR21547–5823	21:58:16	–58:09:40	0.165	12.0	Double
uf3	IR22206–2715	22:23:29	–27:00:03	0.132	12.1	Multiple
u21	IR22491–1808	22:51:49	–17:52:24	0.078	12.0	Multiple
uf5	IR22546–2637	22:57:24	–26:21:13	0.164	11.9	Double
u22	IR23128–5919	23:15:47	–59:03:14	0.044	11.8	Double
u97	IR23140+0348	23:16:35	04:05:17	0.220	12.1	Single

Table 1—Continued

No.	Target name	RA(2000)	Dec(2000)	Redshift <sup>a</sup>	$\log \frac{L_{\text{fir}}}{L_{\odot}}$ <sup>b</sup>	Classification
uf6	IR23146–1116	23:17:14	–11:00:37	0.101	11.8	Double
u98	IR23220+2919	23:24:28	29:35:39	0.241	12.3	Double
u23	IR23230–6926	23:26:04	–69:10:19	0.106	12.1	Single
uf7	IR23242–0357	23:26:50	–03:41:06	0.189*	11.8	Single
u56	IR23365+3604	23:39:01	36:21:08	0.065	12.0	Single
uf8	IR23410+0228	23:43:40	02:45:04	0.092	11.8	Double
uf9	IR23515–2421	23:54:10	–24:04:25	0.153	11.9	Multiple

<sup>a</sup>Redshifts for most targets are from the PSCz catalogue, with some exceptions from on-line NED database (marked by an asterisk).

<sup>b</sup>Far infrared luminosities were calculated from the following expression (Sanders & Mirabel 1996)

$$F_{\text{fir}} = 1.26 \times 10^{-14} \{2.58 f_{60} + f_{100}\} [\text{W m}^{-2}],$$

$$L_{\text{fir}} = L(40 - 500 \mu\text{m}) = 4\pi D_L^2 C F_{\text{fir}} [L_{\odot}],$$

where  $D_L$  is the luminosity distance, the scale factor  $C$  is adopted as 1.6, and  $f_{60}$  and  $f_{100}$  are the  $60 \mu\text{m}$  and  $100 \mu\text{m}$  fluxes from the PSCz catalogue, respectively.

Table 2. Photometric uncertainties in simulated overlapping clumps.

Run No. <sup>a</sup>	Actual $\Delta m_I$ (mag)	Separation (pixel)	Measured $\Delta m_I$ (mag)	uncertainty (mag)
1	0.0	8	0.14	0.08
2	0.0	6	0.19	0.06
3	0.0	4	0.05	0.03
4	0.2	8	0.09	0.06
5	0.2	6	0.38	0.08
6	0.2	4	0.05	0.02
7	0.5	8	0.72	0.17
8	0.5	6	0.57	0.09
9	0.5	4	0.30	0.07
10	1.0	8	1.14	0.22
11	1.0	6	0.85	0.01
12	1.0	4	0.51	0.04

<sup>a</sup>Each parameter combination ( $\Delta m_I$  and separation) consists of ten independent realizations, in which the magnitude of one artificial clump is selected to range from 16.0 mag to 17.8 mag, with a step of 0.2 mag, and the magnitude of the other artificial clump is determined by adding the corresponding  $\Delta m_I$ . Measured  $\Delta m_I$  is the mean value of these ten processes, and the uncertainty refers to the corresponding root mean square error. In all the simulation runs with different flux ratios, the two artificial clumps are always too severely overlapped to be distinguished from each other as their separation drops to around 3 pixel, thus we choose the minimum simulated separation to be 4 pixel; on the other hand, as the clump separation is larger than around 8 pixel, the two clumps in any of the realizations are so well-separated that their fluxes can be determined precisely by applying standard aperture photometry programs, thus the maximum simulated separation of 8 pixel is chosen.

Table 3. Properties of putative nuclei in multiple mergers.

Target name	$\Delta RA''$	$\Delta Dec''$	$M_I$ (mag)	$\frac{L}{L_{\max}}^a$	$S_{\min}$ (kpc) <sup>b</sup>	$L_{\text{tail}}$ (kpc) <sup>c</sup>	Morphology	Spectral type
IR00161–0850	0.12	0.15	–17.95	0.40	0.57	40	tail	LINER
	–0.71	–0.48	–18.94	1.00				
	–0.85	–0.46	–18.62	0.74				
IR02364–4751	0.22	–0.48	–19.10	1.00	0.54	48	tail	
	0.86	–0.30	–18.61	0.64				
	1.01	–0.28	–17.98	0.64				
IR03538–6432	–0.27	0.89	–22.37	1.00	1.91	38	tail, plume	Sy2
	–0.49	0.80	–20.86	0.25				
	–0.77	0.96	–21.16	0.33				
IR04384–4848	0.35	0.47	–18.45	0.40	0.85		plume	H II
	0.47	0.45	–19.31	0.88				
	0.65	0.43	–19.45	1.00				
IR13539+2920	–0.16	–0.65	–17.95	0.08	2.16		plume	H II
	1.21	–1.28	–18.96	0.20				
	1.65	–0.95	–20.69	1.00				
IR14060+2919	–0.17	–1.17	–20.08	1.00	0.51	12	tail, ring	H II
	0.03	–1.06	–19.88	0.83				
	0.15	–1.07	–18.80	0.31				
IR14202+2615	–0.17	–0.02	–18.83	0.65	2.23		arm	H II
	0.16	0.55	–19.30	1.00				
	0.21	0.20	–19.07	0.81				
	2.70	–0.67	–19.05	0.79				
IR14575+3256	1.32	–1.14	–18.35	0.19	1.01		arm	
	1.77	–0.88	–20.16	1.00				
	1.76	–0.63	–19.12	0.38				
IR16007+3743	0.81	–1.26	–19.35	0.35	8.13	18	tail, plume	
	0.44	–0.33	–20.49	1.00				
	0.06	0.69	–20.46	0.97				
IR18580+6527	–0.13	1.49	–18.90	0.19	0.95		ring, plume	Sy2
	0.35	0.78	–20.70	1.00				
	0.21	0.69	–19.83	0.45				
	0.29	0.52	–20.50	0.83				
IR20037–1547	–0.05	0.25	–19.69	0.39	1.12		star-like, ring	QSO
	–1.25	–0.51	–19.50	0.04				
	–1.23	–0.70	–18.90	0.03				
IR20100–4156	–0.25	–0.87	–22.90	1.00	1.55		plume	H II
	1.87	–0.48	–17.48	0.28				
	1.29	–0.12	–18.12	0.50				
	1.22	1.24	–18.30	0.59				
IR20253–3757	0.90	1.11	–18.87	1.00	0.64		ring, plume	H II
	1.26	0.56	–19.77	0.88				
	0.88	1.37	–18.57	0.29				
	0.99	1.47	–19.72	0.84				
	1.09	1.51	–19.91	1.00				
IR21130–4446	1.35	1.67	–18.68	0.32	0.60		ring	H II
	1.10	–1.18	–18.46	0.14				
	0.80	–1.13	–17.96	0.09				
	0.62	–1.27	–17.59	0.06				
	0.44	–1.26	–18.26	0.12				
IR22206–2715	–0.20	–2.05	–18.48	0.15	1.17	25	tail, plume	H II
	–0.14	–2.32	–20.56	1.00				
	0.26	0.35	–18.31	0.21				

Table 3—Continued

Target name	$\Delta RA''$	$\Delta Dec''$	$M_I$ (mag)	$\frac{L}{L_{\max}}^a$	$S_{\min}$ (kpc) <sup>b</sup>	$L_{\text{tail}}$ (kpc) <sup>c</sup>	Morphology	Spectral type
	–0.56	–1.24	–20.03	1.00				
	–0.81	–1.32	–19.83	0.83				
IR22491–1808	–0.48	–1.00	–17.71	0.20	1.22	11	tail, plume	H II
	–0.51	–0.72	–19.44	1.00				
	–1.32	–0.48	–17.95	0.25				
IR23515–2421	–0.09	0.15	–19.84	1.00	0.92	16	tail	LINER
	0.30	0.24	–19.53	0.75				
	0.15	0.35	–19.67	0.86				

<sup>a</sup>The  $I$ -band luminosity ratio of each nucleus to the brightest one in the same target.

<sup>b</sup>The projected minimum nuclear separation.

<sup>c</sup>The projected visible length of the tidal tail.

Table 4. Properties of putative nuclei in pair mergers.

Target name	$\Delta RA''$	$\Delta Dec''$	$M_I$ (mag)	$\frac{L}{L_{\max}}^a$	$S_{\min}$ (kpc) <sup>b</sup>	$L_{\text{tail}}$ (kpc) <sup>c</sup>	Morphology <sup>d</sup>	Spectral type
IR00060–1543	–0.48	0.56	–20.04	0.85	1.84	18	tail	
	–0.32	0.41	–20.22	1.00				
IR00105–0139	–0.69	0.21	–19.45	0.47	4.47	17	tail, plume	
	–1.51	0.40	–20.27	1.00				
IR00150+4937	–0.62	0.37	–19.47	1.00	9.03	20	ring, tail	H II
	–0.53	–1.45	–17.16	0.12				
IR00204+1029	0.91	1.23	–21.94	1.00	1.92	11	tail	Sy1
	0.87	0.95	–19.66	0.12				
IR00461–0728	–1.00	0.63	–20.37	1.00	2.06	16	tail	
	–1.03	0.34	–18.41	0.16				
IR00589–0352	–1.38	0.08	–20.33	1.00	13.83	17	tail	
	0.94	0.90	–19.27	0.38				
IR02459–0233	–0.92	–0.68	–20.49	1.00	5.91		plume	
	–0.45	0.24	–20.00	0.64				
IR05120–4811	–0.50	–0.87	–18.47	1.00	0.67		plume	LINER
	–0.55	–0.75	–17.80	0.54				
IR06035–7102	1.24	1.44	–19.69	0.74	8.65	18	tail, plume	
	–1.42	0.13	–20.01	1.00				
IR06206–6315	0.60	0.16	–17.96	1.00	3.76	18	tail	
	1.19	1.13	–17.71	0.79				
IR06268+3509	–0.58	1.31	–19.40	0.54	8.11	18	tail	H II
	1.28	0.00	–20.06	1.00				
IR06487+2208	–1.44	0.20	–19.59	0.81	1.48		plume	H II
	–1.72	0.08	–19.82	1.00				
IR06561+1902	–0.63	0.67	–20.49	1.00	6.53		plume	LINER
	–0.41	–0.42	–19.34	0.35				
IR08201+2801	0.78	–0.49	–20.06	1.00	6.01	23	tail	H II
	0.29	0.51	–17.68	0.11				
IR08344+5105	0.22	0.18	–19.03	1.00	2.71		ring, plume	
	0.84	0.65	–17.69	0.29				
IR09039+0503	–0.48	–0.28	–19.18	0.95	1.07	28	tail, plume	LINER
	–0.62	0.28	–19.24	1.00				
IR11087+5351	1.06	–1.52	–19.62	0.69	1.18		ring, plume	Sy1
	1.25	–1.67	–20.03	1.00				
IR11095–0238	–0.42	0.97	–18.54	1.00	1.23	18	tail	LINER
	–0.17	1.19	–17.98	0.60				
IR12112+0305	0.08	–0.03	–18.66	1.00	3.74	32	tail, bridge	
	–0.85	–1.05	–17.45	0.33				
IR12490–1009	–1.05	–0.09	–19.87	1.00	2.89		ring, plume	
	–0.30	0.20	–18.08	0.19				
IR13352+6402	–0.75	–1.25	–18.64	0.64	11.49	19	tail	
	0.47	–0.13	–19.13	1.00				
IR13428+5608	–0.07	–1.53	–18.15	1.00	0.36	>31	tail	Sy2
	0.11	–1.37	–17.72	0.67				
IR13469+5833	1.25	–0.33	–19.74	1.00	3.97		arm	
	0.50	–0.46	–17.57	0.14				
IR14312+2825	1.60	–1.41	–20.78	1.00	6.84		ring, plume	Sy2
	0.93	–2.42	–18.55	0.13				
IR14348–1447	–1.03	–0.01	–19.31	1.00	4.83	15	tail	LINER
	–1.87	–1.36	–17.43	0.18				
IR16541+5301	1.00	1.48	–20.13	1.00	5.60			Sy2
	0.50	0.70	–18.62	0.25				

Table 4—Continued

Target name	$\Delta RA''$	$\Delta Dec''$	$M_I$ (mag)	$\frac{L}{L_{\max}}^a$	$S_{\min}$ (kpc) <sup>b</sup>	$L_{\text{tail}}$ (kpc) <sup>c</sup>	Morphology <sup>d</sup>	Spectral type
IR19254–7245	0.23	0.15	–20.17	1.00	8.79	>28	tail	Sy2
	1.01	–3.55	–19.42	0.50				
IR19561–4756	0.39	1.59	–18.94	0.45	1.55	18	tail, plume	
	0.22	1.32	–19.80	1.00				
IR20087–0308	–0.17	–1.39	–17.49	0.81	0.76		plume	LINER
	0.04	–1.38	–17.72	1.00				
IR20314–1919	–0.71	–1.56	–19.95	1.00	4.98		plume	H II
	–1.67	–1.77	–18.45	0.25				
IR20507–5412	–0.67	1.21	–20.25	1.00	1.27			LINER
	0.20	–1.94	–20.23	0.98				
IR20551–4250	–0.07	2.14	–19.45	1.00	0.88	25	tail, plume	H II
	–0.10	–2.66	–18.61	0.46				
IR21547–5823	–1.04	–2.68	–19.40	0.77	14.01	30	tail, plume	LINER
	2.70	–2.44	–19.69	1.00				
IR22546–2637	0.33	0.84	–20.32	1.00	4.67		plume	H II
	–0.18	0.13	–19.19	0.35				
IR23128–5919	0.64	0.10	–17.93	0.75	3.79	17	tail, plume	
	0.80	–2.06	–18.24	1.00				
IR23146–1116	5.92	–1.77	–19.69	1.00	1.77	54	tail	
	6.39	–1.86	–17.89	0.19				
IR23220+2919	0.39	0.61	–18.64	0.13	1.84			H II
	0.20	0.78	–20.85	1.00				
IR23410+0228	–0.52	–0.87	–20.23	1.00	2.78		plume	Sy1
	–1.33	–0.65	–17.51	0.08				

<sup>a</sup>The  $I$ -band luminosity ratio of each nucleus to the brightest one in the same target.

<sup>b</sup>The projected minimum nuclear separation.

<sup>c</sup>The projected visible length of the tidal tail (tidal tails in IR13428+5608 and IR19254–7245 are beyond the FOV of the snapshot images, therefore the tail lengths given here are lower limit values).

<sup>d</sup>Blank line in this column refers to no detectable interacting signatures.

Table 5. Properties of putative nuclei in single nucleus galaxies.

Target name	$\Delta RA$ (")	$\Delta Dec$ (")	$M_I$ (mag)	$L_{\text{tail}}$ (kpc) <sup>a</sup>	Morphology <sup>b</sup>	Spectral type
IR00275–2859	–0.68	0.00	–23.14	8	tail	Sy1
IR00335–2732	0.98	–1.37	–20.44		arm	
IR00509+1225	–1.00	–1.31	–21.67		star-like, arm	Sy1
IR01031–2255	0.82	–0.47	–20.27	17	tail, plume	
IR02054+0835	–0.97	–1.22	–23.46		star-like	Sy1
IR04024–8303	0.31	–1.25	–21.75		star-like, arm	Sy1
IR04413+2608	1.30	1.11	–19.93		arm	Sy2
IR05116+7745	–0.28	–0.05	–19.77			
IR05233–2334	0.40	0.95	–20.02		arm	
IR06361–6217	1.19	0.53	–20.32	4	tail	H II
IR07246+6125	–0.33	–1.17	–20.43			Sy2
IR07381+3215	–0.48	–0.06	–20.60			Sy2
IR08509–1504	–0.09	1.03	–18.48		arm	
IR09320+6134	1.08	–0.42	–18.31			Sy1.5
IR09425+1751	1.08	1.01	–20.78			Sy2
IR09427+1929	0.44	0.91	–21.37		star-like, plume	Sy1
IR10026+4347	0.98	–0.31	–22.49		star-like	Sy1
IR10122+4943	0.89	0.31	–18.23			LINER
IR10558+3845	0.68	–0.20	–20.60		plume	H II
IR10579+0438	–0.02	0.40	–19.60		plume	LINER
IR12108+3157	1.35	–0.18	–19.98		plume	H II
IR12202+1646	1.09	0.19	–21.96			LINER
IR13144+2356	0.41	–0.04	–19.51		plume	
IR13342+3932	0.08	–2.05	–22.60		star-like, arm	Sy1
IR13442+2321	1.75	1.13	–18.65			
IR14170+4545	0.84	–1.28	–20.01		plume	
IR14337–4134	–1.39	–0.69	–21.67		star-like	
IR14378–3651	3.51	–0.53	–19.41			Sy2
IR15413–0959	–0.50	–0.53	–19.75			
IR16159–0402	1.22	–0.43	–21.43			
IR16455+4553	–0.72	–0.18	–19.94		plume	
IR17179+5444	–0.97	–0.47	–20.03			
IR17431–5157	1.85	1.63	–19.79			LINER
IR17463+5806	–0.71	–0.93	–21.09		plume	Sy2
IR19297–0406	–0.66	–0.30	–18.28		plume	H II
IR20109–3003	0.74	–0.70	–19.57		plume	
IR20176–4756	–1.37	1.88	–19.42		arm	
IR20414–1651	–0.24	–0.66	–20.12			H II
IR23140+0348	0.05	–1.36	–21.66		plume	LINER
IR23230–6926	–0.37	–1.18	–19.18		plume	
IR23242–0357	–1.38	–0.88	–20.50		arm	
IR23365+3604	–0.73	–0.63	–18.15			LINER

<sup>a</sup>The projected visible length of the tidal tail.

<sup>b</sup>Blank line in this column refers to regular elliptical morphology.

Table 6. Spectral information for different ULIRG populations.<sup>a</sup>

Spectral type	Single remnants	Double mergers	Multiple mergers
Seyfert 1/QSO	28%	13%	7%
Seyfert 2/LINER	52%	52%	29%
H II	20%	35%	64%

<sup>a</sup>The fraction of galaxies with available spectral information is 82% (14/17), 61% (23/38) and 60% (25/42) for multiple, double and single nucleus/nuclei ULIRGs, respectively.

## Figure captions

Fig. 1.—  $I$ -band magnitude distribution of 57 star-forming knots in the warm ULIRG sample (Surace *et al.* 1998), which are visually fainter than 22.5 mag (i.e., the minimum clump flux in our reduction). The bin width is 0.5 mag. The data in the plot are cited from the literature.

Fig. 2.— Snapshot image, surface and contour plots for IR00161–0850. Scale ruler is 5 kpc in the snapshot image and contour plot. This galaxy consists of two components, of which the northeastern one contains one nucleus and the southwestern one contains two closely separated nuclei. A long tidal tail is clearly seen in the snapshot image.

Fig. 3.— Snapshot image, surface and contour plots for IR02364–4751. Scale ruler is 15 kpc in the snapshot image and 5 kpc in the contour plot. The nuclear region of this galaxy mainly contains two parts, the western part encompasses a bright nucleus and the eastern part encompasses a close nucleus pair. A distinct tidal tail and a faint plume structure can be seen in the system.

Fig. 4.— Snapshot image, surface and contour plots for IR03538–6432. Scale ruler is 15 kpc in the snapshot image and 5 kpc in the contour plot. Morphological and spectral features of this galaxy is like those of the well-known Mrk 273. The central star-like object consists of three separate nuclei, and is connected with a very long tidal tail.

Fig. 5.— Snapshot image, surface and contour plots for IR04384–4848. Scale ruler is 15 kpc in the snapshot image and 5 kpc in the contour plot. This galaxy has a complex morphology which consists of three bright nuclei in the center and four plume structures with much different properties, such as length, intensity, and alignment.

Fig. 6.— Snapshot image, surface and contour plots for IR13539+2920. Scale ruler is 5 kpc in the snapshot image and contour plot. This is a galaxy with relatively weak interacting features. The big, bright object to the southeast is in fact composed of two separate nuclei.

Fig. 7.— Snapshot image, surface and contour plots for IR14060+2919. Scale ruler is 5 kpc in the snapshot image and 1 kpc in the contour plot. Three putative nuclei closely distribute in the central region of the system. Distinct tidal tail as well as ring structure can be seen in the snapshot image.

Fig. 8.— Snapshot image, surface and contour plots for IR14202+2615. Scale ruler is 5 kpc in the snapshot image and contour plot. This system contains two parts, of which the northwestern one consists of three separate nuclei. Two arm structures can be seen clearly from the snapshot image. In contour and surface plots, we only display the northwestern part of this system to get a clearer view.

Fig. 9.— Snapshot image, surface and contour plots for IR14575+3256. Scale ruler is 5 kpc in the snapshot image and 1 kpc in the contour plot. This is a multiple nuclei ULIRG with moderate interacting features.

Fig. 10.— Snapshot image, surface and contour plots for IR16007+3743 . Scale ruler is 10 kpc in the snapshot image and 5 kpc in the contour plot. This galaxy consists of three distinct components, each of which encompasses a bright nucleus. Tidal tail and plume structures can be clearly seen in the system.

Fig. 11.— Snapshot image, surface and contour plots for IR18580+6527 . Scale ruler is 5 kpc in the snapshot image and 1 kpc in the contour plot. This is a typical example of interacting group with complex merging history. The other three bright objects along the tidal ring are foreground stars. The faintest nucleus locates at the north. Although it is not so compact as the other four putative nuclei, its *I*-band absolute magnitude of nearly  $-19.0$  suggests that it is not very likely to be a star cluster association.

Fig. 12.— Snapshot image, surface and contour plots for IR20037–1547 . Scale ruler is 5 kpc in the snapshot image and contour plot. This ULIRG is an example of QSO hosted in an interacting galaxy system. Although the two clumps to the northwest of the system are not very compact, their high luminosities as well as the existence of a distinct tidal ring suggest that they cannot be explained as star-forming knots. Ceiling values are applied in contour and surface plots to display clearly faint structures of the system.

Fig. 13.— Snapshot image, surface and contour plots for IR20100–4156 . Scale ruler is 5 kpc in the snapshot image and contour plot. This galaxy contains two main parts, each of which encompasses two close nuclei. Tidal plumes can be seen connected with each part.

Fig. 14.— Snapshot image, surface and contour plots for IR20253–3757 . Scale ruler is 5 kpc in the snapshot image and contour plot. The northern part contains a single nucleus while the southern part is composed of four separate nuclei. This is a system with relatively weak interacting features.

Fig. 15.— Snapshot image, surface and contour plots for IR21130–4446 . Scale ruler is 5 kpc in the snapshot image and contour plot. This is an interacting system with very peculiar morphologies. Four putative nuclei distribute along a ring structure, while the other two nuclei are away from the ring plane.

Fig. 16.— Snapshot image, surface and contour plots for IR22206–2715 . Scale ruler is 5 kpc in the snapshot image and contour plot. This galaxy mainly contains two parts connected by a tidal bridge. The northeastern part encompasses a single nucleus, while the southwestern one encompasses a close nucleus pair. A straight tail and two plume structures can be seen from the snapshot image.

Fig. 17.— Snapshot image, surface and contour plots for IR22491–1808 . Scale ruler is 5 kpc in the snapshot image and 1 kpc in the contour plot. This is a merging system with three putative nuclei, and the central nucleus is much brighter than the other two. In surface and contour plots, ceiling values are applied to display clearly the structures of the two faint nuclei, as well as star-forming knots. Another bright object clearly seen from surface and contour plots is more likely to be a

foreground star.

Fig. 18.— Snapshot image, surface and contour plots for IR23515–2421 . Scale ruler is 5 kpc in the snapshot image and contour plot. Three putative nuclei of this system concentrate in the center and are very close to each other. The tidal tail can be seen clearly stretching to the southeast.

Fig. 19.— *I*-band magnitude distribution of putative nuclei for the whole sample and the three categories, respectively, as indicated by the labels. The bin width is 0.25 mag for each plot.

Fig. 20.— Distribution of separations between putative nuclei. The upper panel presents distributions of minimum projected nuclear separations of our measurements, while the lower panel presents results from the literature, in which all the separation values have been re-scaled to  $H_0 = 75 \text{ km s}^{-1} \text{ Mpc}^{-1}$ . The bin width is 500 pc for each plot.

Fig. 21.— Correlation between projected nuclear separations and tidal lengths, in which targets of different categories are marked with different symbols. For multiple nuclei systems, minimum nuclear separations are adopted. Several targets with tidal tails extending beyond the image FOV are excluded here.

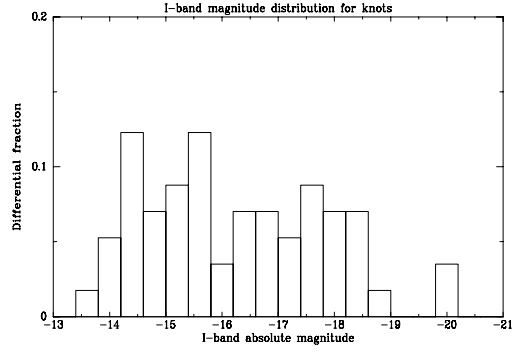


Fig. 1.—

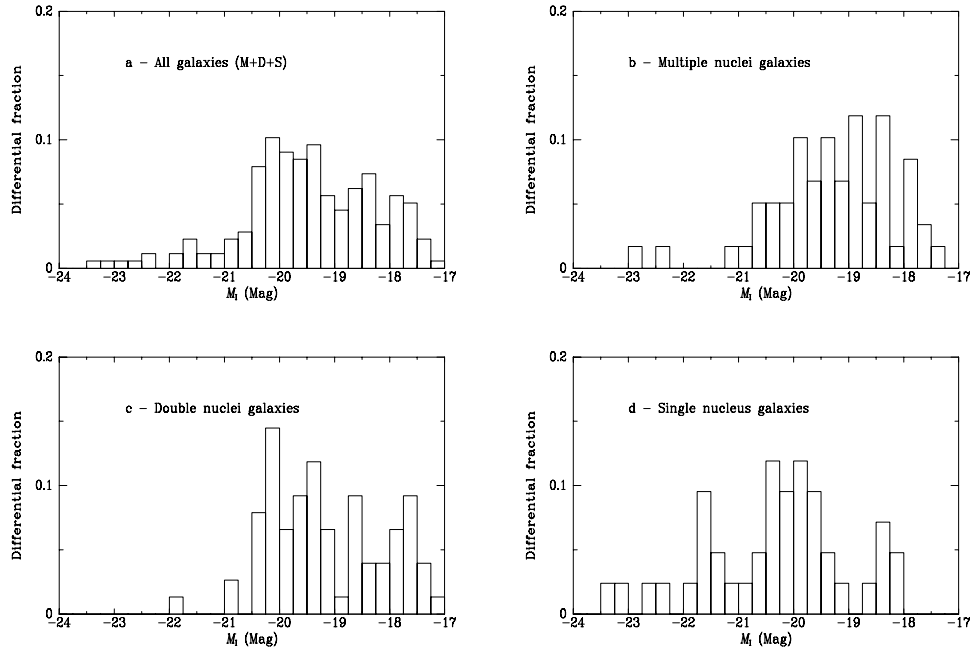


Fig. 2.—

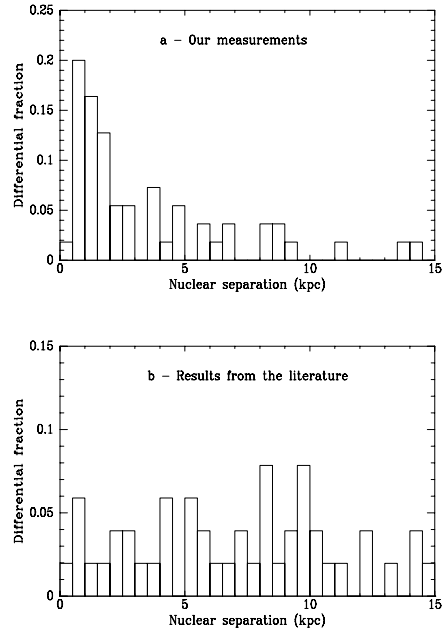


Fig. 3.—

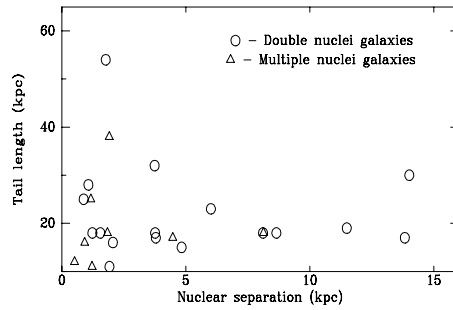


Fig. 4.—

This figure "Cui.fig2.gif" is available in "gif" format from:

<http://arxiv.org/ps/astro-ph/0104296v1>

This figure "Cui.fig3.gif" is available in "gif" format from:

<http://arxiv.org/ps/astro-ph/0104296v1>

This figure "Cui.fig4.gif" is available in "gif" format from:

<http://arxiv.org/ps/astro-ph/0104296v1>

This figure "Cui.fig5.gif" is available in "gif" format from:

<http://arxiv.org/ps/astro-ph/0104296v1>

This figure "Cui.fig6.gif" is available in "gif" format from:

<http://arxiv.org/ps/astro-ph/0104296v1>

This figure "Cui.fig7.gif" is available in "gif" format from:

<http://arxiv.org/ps/astro-ph/0104296v1>

This figure "Cui.fig8.gif" is available in "gif" format from:

<http://arxiv.org/ps/astro-ph/0104296v1>

This figure "Cui.fig9.gif" is available in "gif" format from:

<http://arxiv.org/ps/astro-ph/0104296v1>

This figure "Cui.fig10.gif" is available in "gif" format from:

<http://arxiv.org/ps/astro-ph/0104296v1>

This figure "Cui.fig11.gif" is available in "gif" format from:

<http://arxiv.org/ps/astro-ph/0104296v1>

This figure "Cui.fig12.gif" is available in "gif" format from:

<http://arxiv.org/ps/astro-ph/0104296v1>

This figure "Cui.fig13.gif" is available in "gif" format from:

<http://arxiv.org/ps/astro-ph/0104296v1>

This figure "Cui.fig14.gif" is available in "gif" format from:

<http://arxiv.org/ps/astro-ph/0104296v1>

This figure "Cui.fig15.gif" is available in "gif" format from:

<http://arxiv.org/ps/astro-ph/0104296v1>

This figure "Cui.fig16.gif" is available in "gif" format from:

<http://arxiv.org/ps/astro-ph/0104296v1>

This figure "Cui.fig17.gif" is available in "gif" format from:

<http://arxiv.org/ps/astro-ph/0104296v1>

This figure "Cui.fig18.gif" is available in "gif" format from:

<http://arxiv.org/ps/astro-ph/0104296v1>